ADVANCED FUNCTIONAL MATERIALS
www.afm-journal.de

Fast Fabrication of High-Performance $CoSb_3$-Based Thermoelectric Skutterudites via One-Step Yb-Promoted Peritectic Solidification

Dou Li, Xiao-Lei Shi, Zhenyu Feng, Meng Li, Jiaxi Zhu, Xiao Ma, Lili Zhang, Hong Zhong, Wei-Di Liu, Shuangming Li, and Zhi-Gang Chen**

As a most promising mid-temperature thermoelectric material, $CoSb_3$-based bulk material exhibits an applicable figure-of-merit (*ZT*) of more than one. However, their fabrication is historically time-consuming due to the long-time solid-state phase transitions from $CoSb_2$ to $CoSb_3$. To overcome this challenge, here, a fast one-step process is developed to fabricate n-type Yb-doped $CoSb_3$ with stable *ZT* of 1.12 at 765 K in <5 h. Experiments confirm Yb promotes peritectic reactions of CoSb + Liquid → $CoSb_2$ and $CoSb_2$ + Liquid → $CoSb_3$, optimizes power factor, and suppresses thermal conductivity. Moreover, the dense grains, induced by the one-step crystallization, result in outstanding mechanical properties with a Young's modulus of 171.4 GPa and a hardness of 8.8 GPa in the Yb-doped $CoSb_3$. This study indicates that the fast one-step fabrication route can effectively promote the practical applications of $CoSb_3$-based thermoelectrics and provide guidance for thermoelectric fabrication via rational phase design.

1. Introduction

Recycling waste heat to electricity in an all-solid way can help humans save fossil energy, and thermoelectric materials and their devices can achieve this goal.[1–3] To illustrate their thermoelectric conversion efficiency, the dimensionless figure-of-merit $ZT = \frac{S^2\sigma}{k} T$ is defined, where $S^2\sigma$ represents the power factor, S is the Seebeck coefficient, σ is the electrical conductivity, κ is the thermal conductivity that is contributed from the electronic (κ_e) and lattice (κ_l) parts by $\kappa = \kappa_e + \kappa_l$, and T is the absolute temperature (K).[4] High *ZT* values usually lead to high thermoelectric energy conversion efficiencies in thermoelectric devices and in turn, developing high-performance thermoelectric materials is of significance.[5] Historically, finely tuning the carrier concentration n values by rational band engineering is widely used to optimize the $S^2\sigma$ and *ZT*;[6] while designing hierarchical micro/nanostructures and introducing multi-dimensional crystal and lattice imperfections are both of importance to lower the κ_l since the κ_l is not sensitive to the n.[7] With the rapid development in computational science and technology, the first-principles density functional theory (DFT) calculations and data science are used to guide the designs of both conventional and new thermoelectric materials.[8–10]

Generally, thermoelectric materials with *ZT* values of >1 are suitable for commercial applications.[11–14] Currently, the development of room-temperature thermoelectric materials is relatively mature, such as Bi_2Te_3-based bulk thermoelectric materials, which have initially achieved commercialization.[15–19] However, most Bi_2Te_3-based bulk materials are used for near-room-temperature applications since their peak *ZT*s are at around these temperatures.[20] Considering that many power generation and refrigeration scenarios are based on higher temperatures such as the mid (400–700 K) and high (700–1000 K) temperatures,[2] developing new thermoelectric materials with peak *ZT*s located in the mid-temperature region is still an urgent need. Till now, many newly developed thermoelectric materials such as SnSe,[21] GeTe,[22] and Cu_2Se[23] have reported high mid-temperature *ZT*s of >1 or even >2. However, these materials usually possess relatively low mechanical properties[2] and are either expensive (such as GeTe) or not stable enough at high temperatures, especially for thermoelectric chalcogenides since Se is easy to volatile[24,25] and these materials may be easily oxidized at high temperatures.[2] Among all reported mid-temperature thermoelectric materials,[2]

D. Li, Z. Feng, J. Zhu, X. Ma, L. Zhang, H. Zhong, S. Li
State Key Laboratory of Solidification Processing
Northwestern Polytechnical University
Xi'an 710072, P. R. China
E-mail: lsm@nwpu.edu.cn
X.-L. Shi, M. Li, W.-D. Liu, Z.-G. Chen
School of Chemistry and Physics
Queensland University of Technology
Brisbane, Queensland 4001, Australia
E-mail: zhigang.chen@qut.edu.au
W.-D. Liu
Australian Institute for Bioengineering and Nanotechnology
The University of Queensland
Brisbane 4072, Australia

The ORCID identification number(s) for the author(s) of this article can be found under https://doi.org/10.1002/adfm.202305269

DOI: 10.1002/adfm.202305269

$CoSb_3$-based skutterudites are recognized as good candidates due to their unique features, such as narrow bandgaps, non-toxicity, high stability, mechanical performance, and high resistance to high-temperature oxidation.[26–29] To further their thermoelectric performance, doping by rational filling atoms such as Y,[10,30–44] La,[45,46] In,[35,37] Ba,[36] and Ce[31,37,47] were introduced. However, the complex peritectic phase transition reaction[48] occurring in Co–Sb alloy makes it difficult to fabricate single-phase $CoSb_3$ with higher *ZT*s. According to the phase diagram[49] of Co–Sb alloy (Figure S1, Supporting Information), when the molar ratio of Co:Sb is 1:3, the peritectic reactions $CoSb + L \rightarrow CoSb_2$ and $CoSb_2 + L \rightarrow CoSb_3$ occur at 936 and 874 °C, respectively. There L indicates the liquid phase. The first peritectic reaction ($CoSb + L \rightarrow CoSb_2$) produces a thin envelope layer of $CoSb_2$ surrounding CoSb, isolating the CoSb and the liquid alloy (Sb rich). Due to the obstruction of the thin envelope $CoSb_2$ layer, the peritectic reaction cannot be finished. The second peritectic solidification ($CoSb_2 + L \rightarrow CoSb_3$) is the transformation process from $CoSb_2$ to $CoSb_3$, which is slow and time-consuming since it involves the solute-solid diffusion process.[34,50] **Figure 1**a illustrates the schematic diagram of phase evolution in the Co–Sb alloy peritectic solidification process. As shown in the Line-2 process, through conventional fabrication routes, the two peritectic reactions could not be completely carried out during the solidification process, resulting in amounts of impurity phases in the final products, including CoSb, $CoSb_2$, and liquid alloy phases (mainly Sb rich).[43,51,52] The existence of these impurity phases dramatically deteriorates the thermoelectric properties of $CoSb_3$ materials.[51,52]

To fabricate single-phase $CoSb_3$-based thermoelectric materials, researchers usually choose the synthesis routes that avoid those two complex peritectic reactions. For example, Co and Sb powders were pretreated by mechanical alloying (MA) and sintered under a vacuum atmosphere using a spark plasma sintering (SPS) technique.[45,52–56] Nevertheless, the MA process consumes a long time for the complete reaction between Co and Sb, and some impurity phases form, leading to a seriously deteriorated σ.[57] Therefore, it's hard to achieve high *ZT*s in this way,[46,57–60] as summarized in Table S1 (Supporting Information). Other studies use the annealing of ingot combined with hot pressing (HP) and/or SPS processes to fabricate single-phase $CoSb_3$.[35,42,44,61,62] However, the kinetic process is considerably slow, and peritectic reactions are almost impossible to carry out in a short time. To guarantee that the primary phase CoSb can be completely transformed into a single skutterudite phase $CoSb_3$, as well as ensure the doping elements can sufficiently diffuse to form a uniform and stable structure, a long annealing time needs. As reported, more than 4 days were needed to prepare Yb-filled skutterudites to complete the melting-quenching-annealing process and in turn, a *ZT* of 1.0 at 723 K.[39] As well, pure-phased $Yb_xCo_{4-y}Fe_ySb_{12}$ was synthesized via a melting-quenching route followed by long-term high-temperature annealing (973 K for one week), which exhibited a maximum *ZT* of 1.34 at 780 K.[40] Furthermore, single-doped $CoSb_3$ was obtained by annealing for up to 14 days.[27,47] These studies required a long annealing time of up to more than one week to eliminate the residual impurity phases during the peritectic reaction process, as summarized in Table S1 (Supporting Information). It is historically difficult to obtain high-purity and high-quality single-phase $CoSb_3$ in a short process and within a short time. Therefore, a new method with less time and energy to obtain pure-phased $CoSb_3$ with acceptable *ZT*s (>1) is critical for practical applications and scientific research.

Here, we originally found that introducing Yb in $CoSb_3$ by an innovatively designed one-step heating-sustaining-cooling process can directly obtain Yb-doped $CoSb_3$ products and cost only <5 h, which is very shorter fabrication time than that of reported studies.[27,35,39,40,45–47,52–62] Moreover, the introduction of Yb can significantly promote the two peritectic reactions including $CoSb + L \rightarrow CoSb_2$ and $CoSb_2 + L \rightarrow CoSb_3$ during the solidification process, and rapidly crystallize the micro/nanosized radial-like grains, leading to the single-phase $CoSb_3$, as illustrated in Figure 1a, Such a one-step process only need <5 h, which is much less than those fabrication time of the reported works (Figure S2, Supporting Information).[27,30–41,45–47,50,52,57,58,63] The as-fabricated single-phase $CoSb_3$ has a maximum *ZT* value (ZT_{max}) of 1.12, which is competitive to that of the reported values (Figure S3 and Table S1, Supporting Information).[27,30–41,45–47,50,52,57,58,63] To highlight our unique process, the performance efficiency is described as the ratio between ZT_{max} and fabrication time (ZT_{max}/time) and compared in Figure 1b, indicating our work has a record-high performance efficiency. More important, our Yb-doped $CoSb_3$ bulk materials have a Young's modulus (*Er*) of 171.4 GPa and a hardness (*H*) of 8.8 GPa, which are better than the reported $CoSb_3$-based works (Figure S4, Supporting Information),[64–66] and much higher than those of other high-performance thermoelectric materials such as Bi_2Te_3 (*Er* = 38.8 GPa and *H* = 1.2 GPa),[67] SnSe (*Er* = 53 GPa and *H* = 2.26 GPa),[68] Cu_2Se (*H* = 0.43 GPa),[69] GeTe (*Er* = 51.2 GPa and *H* = 2 GPa),[70] and Cu_3SbSe_4 (*H* = 0.65 GPa),[71] as summarized by Figure 1c.[67–69,71–82] Such outstanding mechanical properties indicate that our materials have great potential for practical applications and future commercialization. The underlying mechanisms for the high thermoelectric and mechanical properties are also illustrated in this study.

2. Results and Discussion

To explore the suitable Yb concentration and achieve $CoSb_3$ with both high thermoelectric performance and less fabrication time, we fabricated six $CoSb_3$-based alloys with different Yb concentrations, described as $Yb_xCo_4Sb_{12}$, namely Co_4Sb_{12} ($CoSb_3$), $Yb_{0.05}Co_4Sb_{12}$, $Yb_{0.1}Co_4Sb_{12}$, $Yb_{0.2}Co_4Sb_{12}$, $Yb_{0.3}Co_4Sb_{12}$, and $Yb_{0.4}Co_4Sb_{12}$. We first studied the fundamentals of adding Yb for achieving a $CoSb_3$ phase during the one-step fabrication processes. In the fabrications of $Yb_xCo_4Sb_{12}$, we all co-heated the precursors (Co, Sb, and Yb single elements) with different Yb contents to 1323 K in a corundum crucible under a protective argon atmosphere within 1 h, sustained at this temperature for 20 min, and cooled to room temperature by a furnace cooling within 2 h. **Figures 2**a–d compare the electron backscattered diffraction (EBSD) phase maps (up) and inverse pole figure (IPF) maps (down) of $Yb_xCo_4Sb_{12}$ (x = 0, 0.1, 0.2, and 0.4). The colors for identifying different phases and orientations via IPF are provided on the right of Figure 2d. A more detailed comparison between the EBSD results of Co_4Sb_{12} and $Yb_{0.2}Co_4Sb_{12}$ are shown in Figure S5 (Supporting Information). As can be seen,

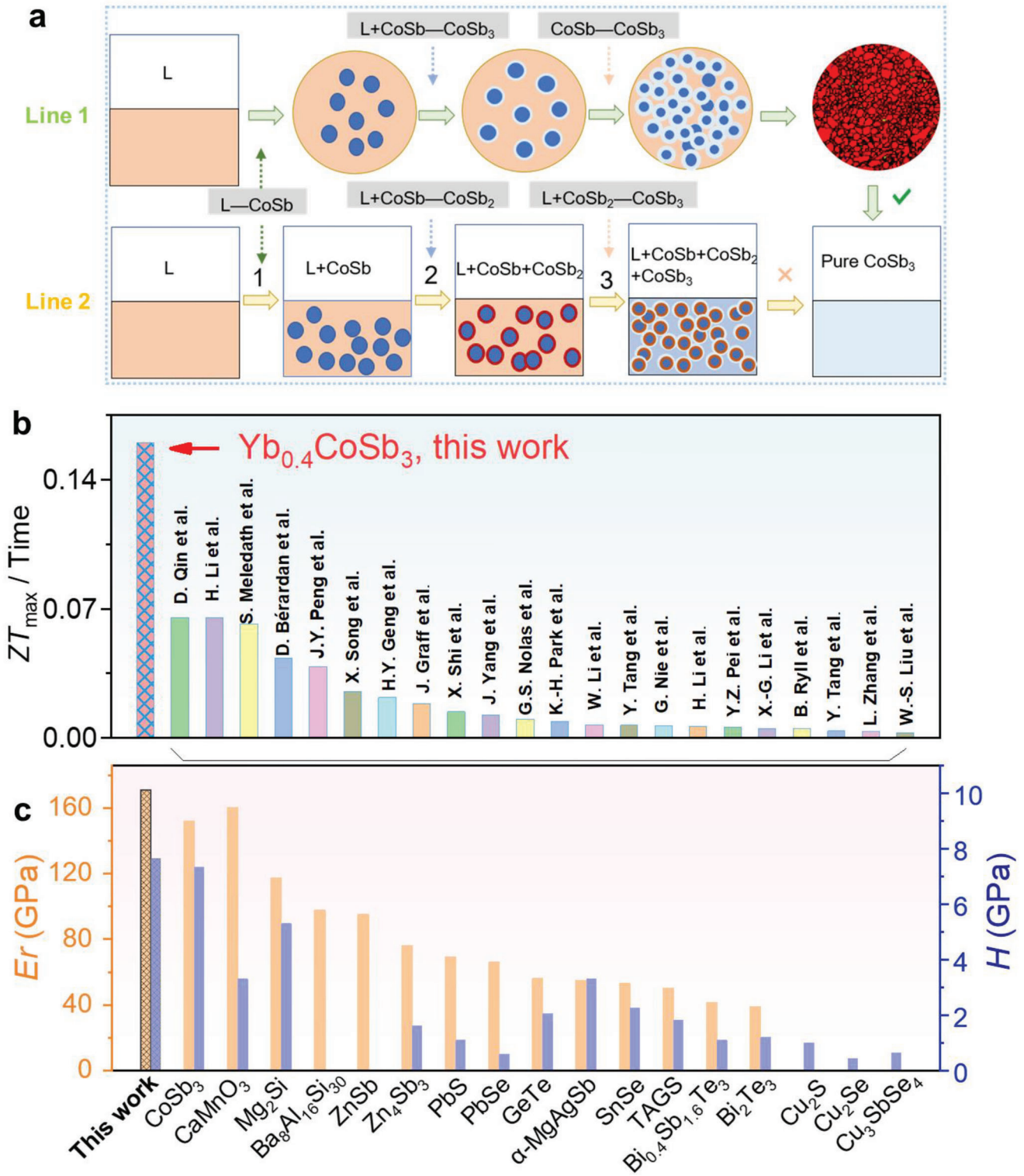

Figure 1. Illustration of peritectic solidification process of Co–Sb alloy and its competitive properties. a) Schematic diagram of phase evolution during Co–Sb alloy peritectic solidification process with and without Yb doping (Lines 1 & 2). b) Comparison of "performance efficiency" (ZT_{max}/time) between this work and reported $CoSb_3$-based works.[27,30–41,45–47,50,52,57,58,63] Here ZT_{max} indicates the maximum ZT. c) Comparison of mechanical properties including Young's modulus Er and hardness H values between this work and reported thermoelectric materials.[67–69,71–82].

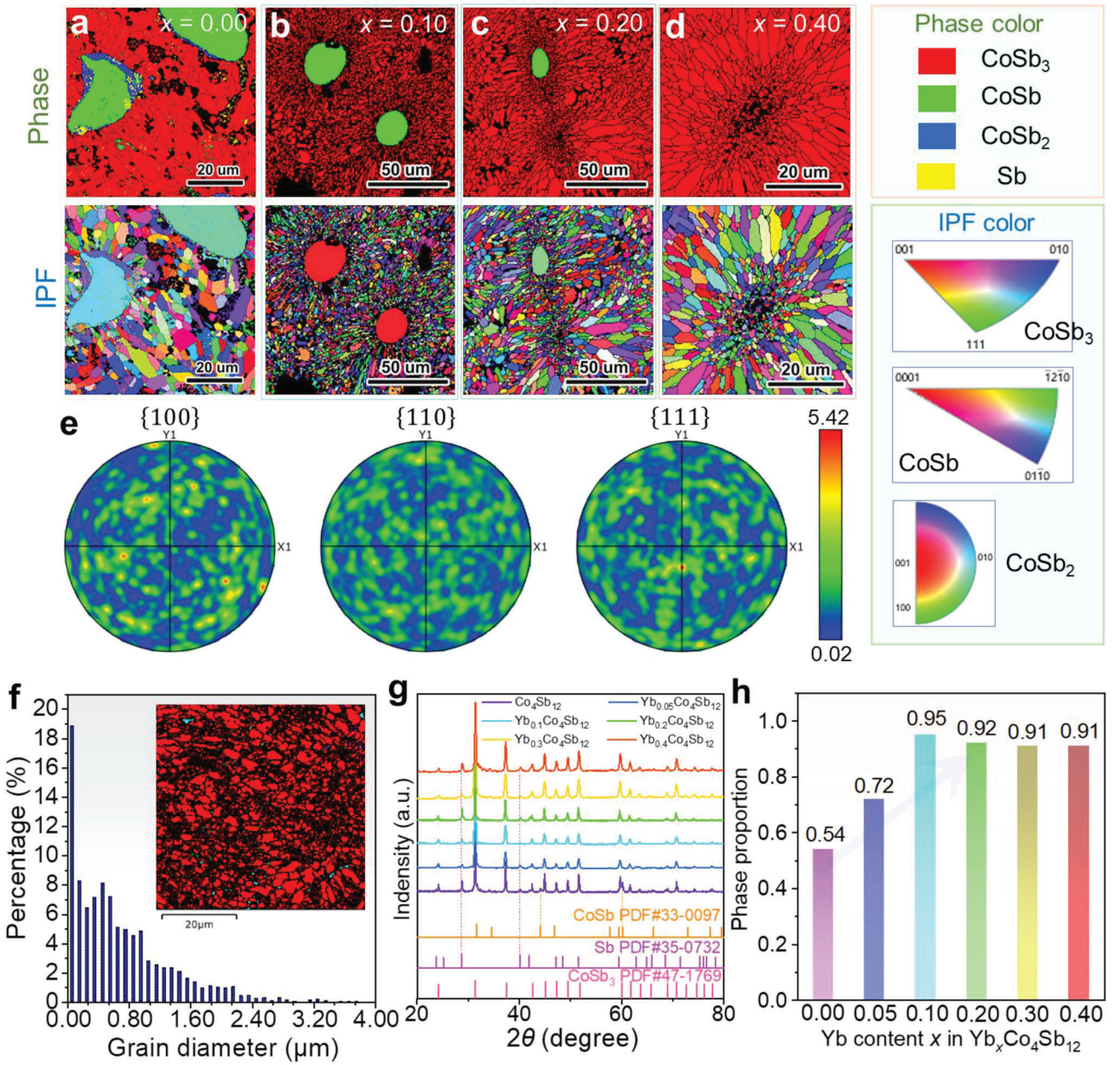

Figure 2. Phase analysis and identification: Electron backscattered diffraction (EBSD) phase maps (up) and inverse pole figure (IPF) maps (down) of $Yb_xCo_4Sb_{12}$ for x = a) 0.00, b) 0.10, c) 0.20, and d) 0.40, respectively. The phase and IPF colors are provided on the right. e) Pole figures of $Yb_{0.4}Co_4Sb_{12}$ for {100}, {110}, and {111} planes. f) Proportions of grain size for $Yb_{0.4}Co_4Sb_{12}$ taken from its EBSD mapping as inset. g) X-ray diffraction (XRD) patterns of $Yb_xCo_4Sb_{12}$ samples for x = 0, 0.05, 0.1, 0.2, 0.3, and 0.4. The 2θ ranges are all from 20 to 80 °. The standard peaks for CoSb, Sb, and $CoSb_3$ phases are included for comparison. h) Proportions of $CoSb_3$ skutterudite phase in $Yb_xCo_4Sb_{12}$ samples.

without introducing Yb, the $CoSb_3$ phase is formed by a conventional two-step way, described as two peritectic reactions including CoSb + L → $CoSb_2$ and then $CoSb_2$ + L → $CoSb_3$. As shown in the EBSD maps of Figure 2a, CoSb phases as cores are covered by $CoSb_2$ phases, which are also covered by $CoSb_3$ phases, confirming the two peritectic reactions. However, the first peritectic reaction (CoSb + L → $CoSb_2$) usually costs more time than the secondary peritectic reaction ($CoSb_2$ + L → $CoSb_3$) to finish the formation of $CoSb_3$ phase,[83] and this is why conventional fabrication routes are considerably time-consuming. In our work, after adding Yb during the as-designed one-step fabrication process, no $CoSb_2$ phase can be found. This suggests that the $CoSb_2$ phases, transferred from the core CoSb phases, can be rapidly transferred to the $CoSb_3$ phases. With increasing the Yb content, fewer core CoSb phases can be found, and when the Yb content reached 0.4, almost no CoSb phase can be found but leaving radial-like grains around the vanished core CoSb phase, indicating that the introduction of Yb can significantly

accelerate the two peritectic reactions without forming $CoSb_2$ phases. Such an interesting phenomenon can be described by the phase diagrams, as shown in Figure S6 (Supporting Information). Figure 2e shows the polar diagrams of EBSD in Figure 2d for {100}, {110}, and {111} planes, from which the grain orientations are isotropic. Figure 2f statistically summarizes the proportions of grain size for $Yb_{0.4}Co_4Sb_{12}$ by analyzing the EBSD results as shown in Figure 2d, from which most of the grains are smaller than 1 μm, indicating that our as-achieved products possess obvious nanograin structures. Besides, we can quantify each phase by the EBSD results (see Table S2, Supporting Information). For example, for the $Yb_{0.2}Co_4Sb_{12}$ sample, there are five phases including $CoSb_3$, CoSb, $CoSb_2$, $YbSb_2$, and Sb, which accounted for 89.63%, 1.02%, 0.26%, 1.30%, and 0.90% respectively. Noted that the zero solution phase of 6.89% can be attributed to the abundant grain boundaries of $CoSb_3$. Therefore, the actual phase fraction of skutterudite $CoSb_3$ should be 96.52% (89.63% + 6.89%), and the real content of the impurity phase is much less than 10% (much closer to 3.42%). In addition to the EBSD results, other characterization methods, such as optical microscopy (OM), can also confirm these results, as shown in Figures S7 and S8 (Supporting Information). Figure 2g compares X-ray diffraction (XRD) patterns of as-achieved $Yb_xCo_4Sb_{12}$ samples. The 2θ ranges are all from 20° to 80°. The standard peaks for CoSb, Sb, and $CoSb_3$ phases are included for comparison. Without adding Yb, there are at least three phases that can be found, namely the $CoSb_3$ phase (major phase), the CoSb phase, and the Sb phase. The Sb phase is a commonly found secondary phase in the $CoSb_3$ system due to its high concentration during the synthesis.[48] With increasing the Yb contents, the peaks for CoSb and Sb phases become less significant, indicating the reduced phase proportions of CoSb and Sb, and the $CoSb_3$-based skutterudite phase start to become the dominant phase. Figure 2h compares the proportions of $CoSb_3$ skutterudite phase in $Yb_xCo_4Sb_{12}$ samples calculated from the optical microscopy (OM) images shown in Figure S8 (Supporting Information) via an Image Pro-Plus (IPP) software, from which when Yb content x increases from 0 to 0.1, the proportion of $CoSb_3$ phase increases from 54% to 95%, indicating rapid phase transitions from CoSb and $CoSb_2$ to $CoSb_3$, and the proportions of the impurity phases are sharply decreased. As the Yb content continues to increase, the proportion of $CoSb_3$ phase is slightly decreased, and finally maintains at ≈91%. However, compared with the results of EBSD (e.g., 96.52% $CoSb_3$ phase for the $Yb_{0.2}Co_4Sb_{12}$ sample), the calculated proportion of $CoSb_3$ phase by OM should be >91% since OM cannot evaluate the abundant grain boundaries of $CoSb_3$. At the same time, it is historically impossible to achieve 100% purity in a $CoSb_3$ system due to its Sb-rich nature during the synthesis. When the Yb content x was >0.1, the decrease in the proportion of the $CoSb_3$ phase results from the precipitation of new phases including Sb and Yb-rich phases, which occupy part of the proportion of the $CoSb_3$ phase, as shown in energy-dispersive X-ray spectrometry (EDS) results (Figures S9–S14, Supporting Information).

To investigate the micro/nanostructural characteristics of the as-fabricated $Yb_xCo_4Sb_{12}$, we performed detailed characterizations based on double spherical aberration-corrected scanning transmission electron microscopy (Cs-STEM) equipped with an EDS detector. **Figure 3**a shows a low-magnification TEM image of the $Yb_{0.4}Co_4Sb_{12}$ prepared by an ion thinning technique, from which micro/nanosized grains can be observed with grain sizes of <2 μm, which are consistent with the results shown in Figure 2f. At the same time, these grains exhibit different contrasts (Figure S15, Supporting Information), indicating different orientations, attributed to the isotropy features of skutterudites. A few nanopores can be simultaneously found between the grains (Figure S15, Supporting Information), which is the nature of polycrystalline $CoSb_3$. Figure 3b shows an indexed selected area electron diffraction (SAED) pattern taken from the square area in Figure 3a (within one grain), from which typical crystalline features can be observed viewed along the $[\bar{1}11]$ direction. Figure 3c shows an atomic-resolution Cs-STEM high-angle annular dark-field (HAADF) image viewed along the [111] direction with an overlapped crystal structure in the center, directly confirming the as-achieved $CoSb_3$ phase as the major phase of the matrix. At the same time, Yb atoms can be found in the interstitial sites of $CoSb_3$, indicating that Yb has been doped in the form of filling behavior and acts as a point defect. The overlapped crystal structure can be referred in Figure S16 (Supporting Information). Figure 3d shows a HAADF image and corresponding EDS maps for Co, Sb, and Yb elements, from which all elements are uniformly distributed, and Yb is further confirmed. The TEM and corresponding SAED images of the $Yb_{0.4}Co_4Sb_{12}$ viewed along the [011], [001], and [111] directions are provided in Figure S17 (Supporting Information). Figure 3e shows a high-resolution TEM (HRTEM) image taken from a highly distorted area as the inset TEM image shows. The highly distorted area induces significant lattice distortions derived from the elemental segregation. Figure 3f shows an HRTEM image taken from the grain boundary area as the inset TEM image shows. Between the three grains with different orientations, the grain boundaries show obvious lattice mismatch, indicating potential lattice distortions or edge-like dislocations, which are embedded around these mismatch areas. Figure 3g shows a HAADF image and corresponding EDS maps for Co, Sb, and Yb elements, from which a Yb-rich secondary phase can be observed. Further EDS spot result (Figure S18, Supporting Information) indicates that such a Yb-rich secondary phase belongs to the $YbSb_2$ phase according to its composition. However, because of its low concentration in the matrix, XRD results are difficult to identify these secondary phases (Figure S19, Supporting Information), and we can only occasionally observe these secondary phases by TEM characterizations such as in the $Yb_{0.2}Co_4Sb_{12}$ (Figure S20, Supporting Information). Figure 3h shows a TEM image with different contrasts between the two phases, and Figure 3i shows an HRTEM image taken from the square area in Figure 3h. The major $CoSb_3$ phase and the $YbSb_2$ secondary phase possess clear boundaries, and the boundary roughness is much lower than that of the grain boundaries. Therefore, there are multi-dimensional crystal and lattice imperfections found in our as-fabricated $Yb_xCo_4Sb_{12}$, which are expected to be beneficial for suppressing their κ.

To further understand the interaction of different phases observed in our as-fabricated $Yb_xCo_4Sb_{12}$ and their expected contribution to the thermoelectric performance, we performed first-principles DFT calculations. **Figures 4**a–f compare calculated band structures of $CoSb_3$ (Co_4Sb_{12}), Yb-filled $CoSb_3$ ($YbCo_4Sb_{12}$), CoSb, $CoSb_2$, Sb, and $YbSb_2$, respectively, which were calculated based on their unit cells (Figures S21–S25, Supporting

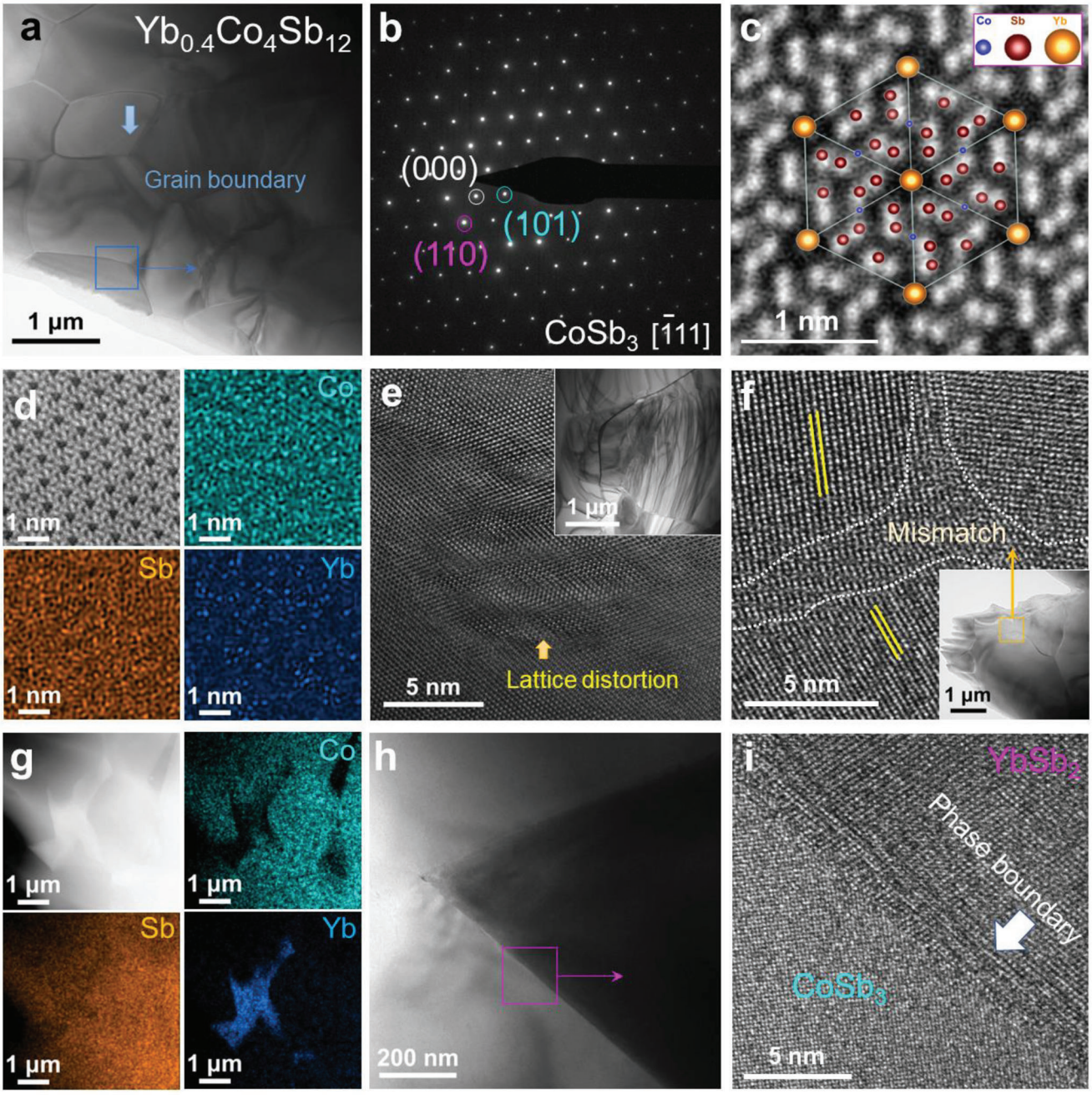

Figure 3. Micro/nanostructure analysis: a) Low-magnification transmission electron microscopy (TEM) image of the $Yb_{0.4}Co_4Sb_{12}$ sample prepared by an ion thinning technique. b) Indexed selected area electron diffraction (SAED) pattern taken from the square area in (a). c) Magnified spherical aberration-corrected scanning transmission electron microscopy (Cs-STEM) high-angle annular dark-field (HAADF) image viewed along the [111] direction with an overlapped crystal structure in the center. d) HAADF image and corresponding energy-dispersive X-ray spectrometry (EDS) maps for Co, Sb, and Yb elements. e) High-resolution TEM (HRTEM) image taken from a highly distorted area as an inset. f) HRTEM image taken from the grain boundary area as inset. g) HAADF image taken on secondary phases and corresponding EDS maps for Co, Sb, and Yb elements. h) TEM image of two phases with different contrasts. i) HRTEM image taken from the square area in (h).

Information). For the pristine $CoSb_3$, it possesses a narrow indirect bandgap of 0.135 eV, indicating that $CoSb_3$ should possess high pristine *n* since the narrow gap allows the carriers to move more easily. For the Yb-filled $CoSb_3$, the band structure of $YbCo_4Sb_{12}$ possesses a direct bandgap instead of an indirect bandgap, and the Fermi level has crossed the conduction band, indicating that electrons are easier to realize charge carrier transition. Such a phenomenon is derived from the filled Yb atoms in the interstitial sites of $CoSb_3$ that can release free electrons as carriers, therefore rational filling Yb can further benefit the n-type electrical transport. In terms of the secondary phases found in the matrix including CoSb, $CoSb_2$, Sb, and $YbSb_2$, as can be

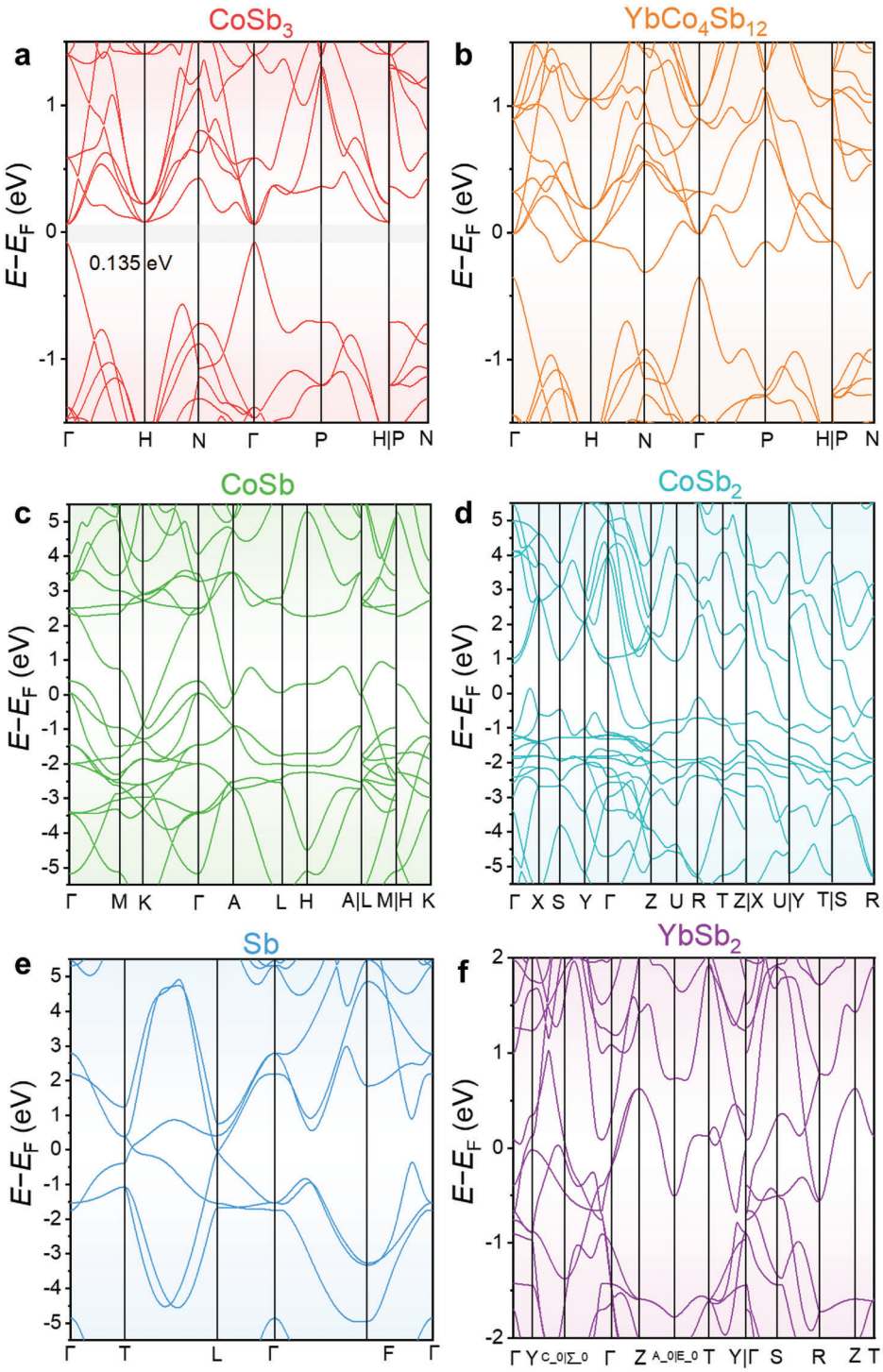

Figure 4. First-principles calculations: Calculated band structures of a) $CoSb_3$ (Co_4Sb_{12}), b) Yb-filled $CoSb_3$ ($YbCo_4Sb_{12}$), c) CoSb, d) $CoSb_2$, e) Sb, and f) $YbSb_2$. Here the calculations for CoSb and $CoSb_2$ consider the spin-down state to be majority spin state.

seen from their band structures, they all exhibit metallic transport behaviors, therefore should benefit the n-type transportation theoretically. However, considering that most of these secondary phases possess much higher κ than that of $CoSb_3$ due to their metallic features,[48,50] and additional metallic phases may also reduce the overall S due to the boosting of n, rationally controlling the concentrations of these secondary phases is required. Besides, considering that CoSb and $CoSb_2$ are materials with certain magnetic features, the calculations for CoSb and $CoSb_2$ (Figures 4c,d) consider the spin-down state to be majority spin

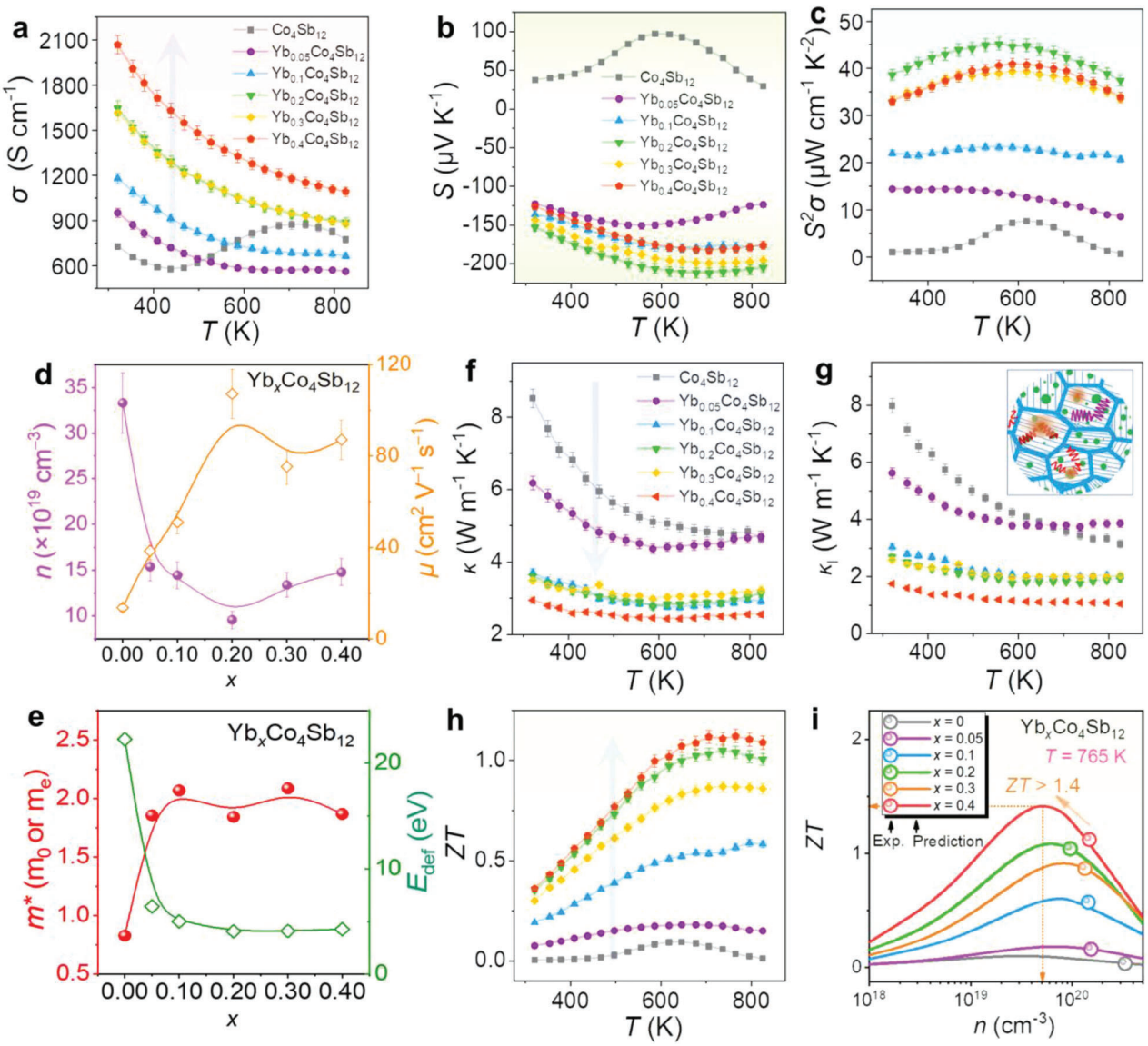

Figure 5. Thermoelectric properties of $Yb_xCo_4Sb_{12}$ for x = 0.00, 0.05, 0.10, 0.20, 0.30, and 0.40: Measured temperature-dependent a) electrical conductivity σ, b) Seebeck coefficient S, and c) power factor $S^2\sigma$. d) Measured carrier concentration n and mobility μ. e) Calculated effective mass m^* and deformation potential E_{def} by a single parabolic band (SPB) model. Temperature-dependent f) thermal conductivity κ, g) lattice thermal conductivity κ_l, and h) ZT. i) Comparison of experimental and calculated ZT as a function of n. The inset in g shows a schematic diagram of phonon scattering sources found in $Yb_xCo_4Sb_{12}$ fabricated by our one-step fabrication route.

state, and the DFT calculations that consider the spin-up state being the minority spin state are shown in Figures S26 and 27 (Supporting Information) for a reference. Nevertheless, both situations indicate typical metallic features of CoSb and $CoSb_2$.

We further investigated the thermoelectric properties of the as-fabricated $Yb_xCo_4Sb_{12}$ (x = 0, 0.05, 0.1, 0.2, 0.3, and 0.4), and the results are plotted in **Figure 5**. Figure 5a presents the temperature-dependent σ and displays a negative slope toward higher temperatures, indicating typical behaviors of heavily doped semiconductors. With increasing the Yb concentration, the σ is gradually increased over the entire temperature range. This is because the filled Yb provides free electrons as carriers for promoting the σ. Figure 5b presents the temperature-dependent S, and the S is negative for the as-fabricated $Yb_xCo_4Sb_{12}$ ($x > 0.00$), showing n-type semiconductor behaviors, and peaks at ≈705 K due to the bipolar diffusion. For the $CoSb_3$ sample without Yb doping, a small amount of Sb phase remained in the product after the solidification process, which is confirmed by Figure S19 (Supporting Information). As shown in Figure S28 (Supporting Information), elemental Sb demonstrates p-type conduction, while the conduction type and ability vary with different amounts of Sb in $CoSb_3$, as depicted in Figure S29 (Supporting Information).[84] Thus, the presence of some Sb phase in $CoSb_3$ is the reason for its p-type conductivity. Besides, with further increasing x from 0.2 to 0.4, the maximum absolute S values decrease from 212 to 182 μV K^{-1} resulting from the increase of n.

Figure 5c shows the determined $S^2\sigma$, from which the highest $S^2\sigma$ were achieved in the $Yb_{0.2}Co_4Sb_{12}$ sample within the temperature range of 300–900 K. To further understand the as-achieved high $S^2\sigma$, Figure 5d compares the measured n and mobility μ. As can be seen, pristine $CoSb_3$ possesses the highest hole carrier concentration n_p (here hole carriers are the major carriers in the system). With increasing the x from 0.05 to 0.2, the electron carrier concentration n_e decreases (here electron carriers are the major carriers in the systems) while the μ increases, which should be resulted from the syngeneic effect of CoSb and $CoSb_2$ secondary phases and Yb-filling. The lowest n_e is observed when $x = 0.2$, explaining the highest S in Figure 5b. With further increasing the x from 0.2 to 0.4, the n_e slightly increases while the μ first decreases and then increases. Such a phenomenon is derived from the fact that when $x > 0.2$, the proportions of CoSb and $CoSb_2$ secondary phases significantly reduce, and Yb-filling starts to play a dominant role in determining the electrical transport behavior. Note that the formation of $YbSb_2$ also contributes to the improvement of n_e. Figure 5e compares the calculated effective mass m^* and deformation potential E_{def} by a single parabolic band (SPB) model. Pristine $CoSb_3$ possesses the lowest m^*, which further explains the lowest S value in Figure 5b. Oppositely, pristine $CoSb_3$ possesses the highest E_{def}, which explains the low μ. With Yb-filling, the m^* was increased while the E_{def} was decreased. The increased m^* indicates that higher S can be achieved due to the potential energy filtering effect between different phases due to their distinct band structures (Figure 4), while the decreased E_{def} explains the overall structural evolution that increased the μ.

Figure 5f shows the temperature-dependent κ of the as-fabricated $Yb_xCo_4Sb_{12}$ materials for $x = 0$, 0.05, 0.1, 0.2, 0.3, and 0.4, respectively. Generally, with increasing temperature, the κ of all samples decreases, indicating typical semiconducting thermal transport behaviors. As well, with increasing the Yb concentration, the κ reduces from 8.5 W m^{-1} K^{-1} in $CoSb_3$ to 2.9 m^{-1} K^{-1} in $Yb_{0.4}Co_4Sb_{12}$ at 320 K, which can be attributed to the removal of metal phases $CoSb_2$ and $CoSb_2$ with much higher κ.[48,50] Figure 5g shows the as-determined κ_l by $\kappa_l = \kappa - \kappa_e$, where the κ_e can be calculated via the Wiedemann–Franz equation by $\kappa_e = L\sigma T$ and L is the Lorenz number calculated by the SPB model.[68] The temperature-dependent κ_e and L are provided in Figure S30 (Supporting Information) for reference. As shown in Figure 5g, with increasing the x, the κ_l is significantly suppressed, which is the result of effective phonon scattering at the introduced crystal and lattice imperfects as observed in Figure 3. The main phonon scattering sources were also summarized in Figure S31 (Supporting Information) for reference. Figure 5h compares the determined ZT. High ZTs of >1 at >600 K, as well as a competitively high peak ZT of 1.12 at 765 K, can be achieved in $Yb_{0.4}Co_4Sb_{12}$. Figure 5i also compares the experimental and calculated ZT as a function of n, from which the calculated ZT was from the SPB modeling. It can be seen that by further suppressing the n to $\approx 5\times10^{19}$ cm^{-3}, a peak ZT of >1.4 can be further realized, which can be realized by further finely tuning the Yb concentration. Nevertheless, our study is non-ZT-orientated and mainly focuses on the design of efficient fabrication of $CoSb_3$-based polycrystals with simultaneously suitable ZTs and mechanical robust features. Also, high repeatability was achieved in our thermoelectric properties (Figure S32, Supporting Information).

Since the thermoelectric materials in the devices need to withstand high external pressure during use, high mechanical properties are simultaneously required. **Figure 6**a shows a scanning electron microscopy (SEM) backscattered electron (BSE) image of the finely polished $Yb_{0.4}Co_4Sb_{12}$ and shows different phase regions for mechanical property measurements. Figure 6b illustrates typical load-displacement nano-indentation curves of CoSb, $CoSb_2$, and $CoSb_3$ phases, indicating a representative brittle fracture feature. Figure 6c compares the H and Er between different phases, which are directly obtained from the curves in Figure 6b. The H and Er values of the $CoSb_2$ phase are significantly lower than those of other phases, and this is why the elimination of the $CoSb_2$ phase is beneficial to improve the overall mechanical properties. Figure 6d shows a microscopic morphology of the nanoindentation directly obtained by the nanoindenter, from which no obvious crack can be found around the nanoindentation, indicating that the as-obtained material is not sensitive to cracking caused by external forces. Such a feature is mainly derived from the isotropic structures of skutterudites. The 3D morphology of the nanoindentation can be referred to Figure S33 (Supporting Information). Figure 6e presents the room-temperature load–displacement nanoindentation curves of the $CoSb_3$ phases of Co_4Sb_{12}, $Yb_{0.2}Co_4Sb_{12}$, and $Yb_{0.4}Co_4Sb_{12}$, while the corresponding H and Er values are plotted in Figure 6f. As can be seen, $Yb_{0.4}Co_4Sb_{12}$ has higher H (8.8 GPa) and E_r (171.4 GPa) at room temperature, which should be attributed to the synergistic effect of the elimination of the mechanically poor impurity phase and the grain size refinement of the matrix phase. Compared with other $CoSb_3$-based works[64–66] as well as many other thermoelectric materials such as Bi_2Te_3,[67] SnSe,[68] Cu_2Se,[69] GeTe,[70] and Cu_3SbSe_4,[71] our H and E_r are much higher, indicating our method is beneficial for fabricating robust thermoelectric devices that target mid- and high-temperature power generation scenarios. To further understand the mechanical properties of the as-fabricated $Yb_{0.4}Co_4Sb_{12}$, a cyclic loading test was performed with variable loads. The maximum load varied from 1 to 10 mN, each load was held for 1 s, the unloading amount was 50% of the maximum load, and the cycle load was 100 times, as shown in Figure 6g and Figure S34 (Supporting Information) (magnified curves). Figure 6h shows the load–displacement curve over 100 cycles of loading. With increasing the loading, the depth of the indentation was deepened, reaching 250 nm at its deepest point. Variations of H and Er with loop loading are shown in Figure 6i. It can be seen that with increasing the number of cyclic loading, both H and Er were decreased. After 100 cycles of variable loading, H was decreased from 8.7 to 7.3 GPa, and Er was decreased from 143 to 119 GPa, leading to a defect structure in the system due to the cyclic deformation. However, the as-achieved sample still has much higher mechanical properties than most inorganic thermoelectric materials. The cyclic loading test at a constant loading also shows excellent mechanical properties of the sample (Figure S35, Supporting Information). For thermoelectric devices, thermoelectric materials as one of the key components play a crucial role in providing stable power output or cooling performance. Therefore, their mechanical performance needs to meet certain requirements to withstand structural damage caused by external forces, such as micro-cracks and poor contact between the material and electrodes. Therefore, considering the comprehensive

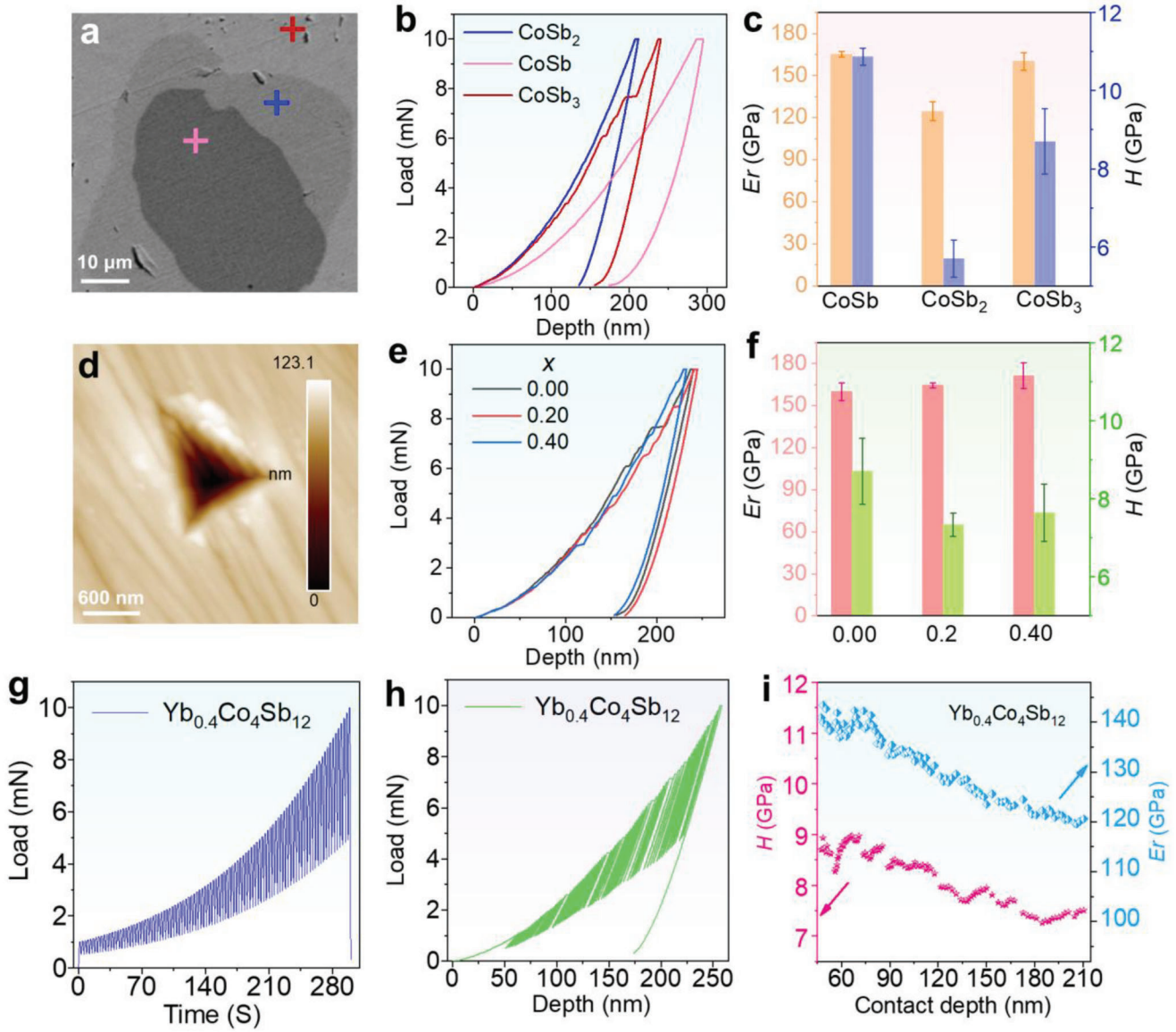

Figure 6. Mechanical properties: a) SEM backscattered electron (BSE) image of a finely polished $Yb_{0.4}Co_4Sb_{12}$ sample to show different phase regions for mechanical property measurements. b) Load-depth curves taken from different phases are shown in (a). c) Comparison of as-achieved hardness *H* and modulus of elasticity *Er* between different phases. d) The microscopic morphology of the nanoindentation obtained by the nano-indenter. e) Load-depth curves taken from the $CoSb_3$ phases for $Yb_xCo_4Sb_{12}$ samples ($x = 0$, 0.2, and 0.4). f) Comparison of as-achieved *H* and *Er* taken the $CoSb_3$ phases for $Yb_xCo_4Sb_{12}$ samples ($x = 0$, 0.2, and 0.4). g) Load function for the cyclic-loading procedure under variable loading. h) Cyclic load-depth curves taken from the $Yb_{0.4}CoSb_3$ sample for 100 times. i) The change of *H* and *Er* with the cyclic loading process.

improvement from aspects of high material fabrication efficiency (Figure S36, Supporting Information), high thermoelectric performance, and high mechanical properties, the discovery of one-step Yb-promoted peritectic solidification holds significant value for material applications and device design optimization.

3. Conclusion

In this work, we report stable *ZT*s of >1 at >600 K in the Yb-filled $CoSb_3$ by a fast heating-sustaining-cooling process, from which the entire fabrication route is much more efficient (within 5 h). We originally found that introducing Yb during the heating process can accelerate the Co–Sb peritectic reaction, leading to nearly single-phase $Yb_xCo_4Sb_{12}$ thermoelectric materials. The metallic intermediate phases such as CoSb and $CoSb_2$ are eliminated, and the radial-like $CoSb_3$ grains are formed. The co-effect of Yb-doping and grain refinement results in low κ_l and high $S^2\sigma$, resulting in such high *ZT*s in a much easier and more efficient way. Meanwhile, the effective removal of the $CoSb_2$ phase and grain refinement by the one-step fabrication significantly improves the mechanical properties of $CoSb_3$, showing significantly high practical application values for fabricating thermoelectric devices that target mid- and high-temperature power generation scenarios. This work exhibits a new way based on novel phase design to

fabricate high-performance thermoelectric materials more efficiently.

4. Experimental Section

The experimental details are provided in the Supporting Information.

Supporting Information

Supporting Information is available from the Wiley Online Library or from the author.

Acknowledgements

D.L. and X.-L.S. contributed equally to this work. This work was supported by the Research Fund of the National Natural Science Foundation of China (51774239), and the Research Fund of the State Key Laboratory of Solidification Processing in NWPU (2022-TS-03). Zhi-Gang Chen thanks the financial support from the Australian Research Council, HBIS-UQ Innovation Centre for Sustainable Steel project, and QUT Capacity Building Professor Program. The authors acknowledge National Computational Infrastructure supported by the Australian government for providing computing resources and technical services.

Open access publishing facilitated by Queensland University of Technology, as part of the Wiley - Queensland University of Technology agreement via the Council of Australian University Librarians.

Conflict of Interest

The authors declare no conflict of interest.

Data Availability Statement

The data that support the findings of this study are available from the corresponding author upon reasonable request.

Keywords

$CoSb_3$, peritectic, skutterudite, thermoelectric, Yb-doping

Received: May 12, 2023
Revised: June 13, 2023
Published online:

[1] G. J. Snyder, E. S. Toberer, *Nat. Mater.* **2008**, *7*, 105.
[2] X.-L. Shi, J. Zou, Z.-G. Chen, *Chem. Rev.* **2020**, *120*, 7399.
[3] Z. Wu, S. Zhang, Z. Liu, E. Mu, Z. Hu, *Nano Energy* **2021**, *91*, 106692.
[4] Q. Yang, S. Yang, P. Qiu, L. Peng, T.-R. Wei, Z. Zhang, X. Shi, L. Chen, *Science* **2022**, *377*, 854.
[5] B. Jiang, W. Wang, S. Liu, Y. Wang, C. Wang, Y. Chen, L. Xie, M. Huang, J. He, *Science* **2022**, *377*, 208.
[6] Y. Pei, H. Wang, G. J. Snyder, *Adv. Mater.* **2012**, *24*, 6125.
[7] X.-L. Shi, W.-Y. Chen, X. Tao, J. Zou, Z.-G. Chen, *Mater. Horiz.* **2020**, *7*, 3065.
[8] F. Li, X. Liu, N. Ma, L. Chen, L.-M. Wu, *Angew. Chem., Int. Ed.* **2022**, *61*, e202208216.
[9] M. Saeidi-Javash, K. Wang, M. Zeng, T. Luo, A. W. Dowling, Y. Zhang, *Energy Environ. Sci.* **2022**, *15*, 5093.
[10] Z. Wang, J. Xi, J. Ning, K. Guo, B. Duan, J. Luo, G. J. Snyder, J. Yang, W. Zhang, *Chem. Mater.* **2021**, *33*, 1046.
[11] S. Y. Tee, D. Ponsford, C. L. Lay, X. Wang, X. Wang, D. C. J. Neo, T. Wu, W. Thitsartarn, J. C. C. Yeo, G. Guan, T.-C. Lee, M.-Y. Han, *Adv. Sci.* **2022**, *9*, 2204624.
[12] T. Cao, X.-L. Shi, Z.-G. Chen, *Prog. Mater. Sci.* **2023**, *131*, 101003.
[13] W.-Y. Chen, X.-L. Shi, J. Zou, Z.-G. Chen, *Mat. Sci. Eng. R* **2022**, *151*, 100700.
[14] L. Zihang, G. Weihong, G. Fengkai, C. Wei, Z. Qian, S. Jiehe, *Mater. Lab.* **2022**, *1*, 220003.
[15] J. Mao, H. Zhu, Z. Ding, Z. Liu, G. A. Gamage, G. Chen, Z. Ren, *Science* **2019**, *365*, 495.
[16] H. Mamur, M. R. A. Bhuiyan, F. Korkmaz, M. Nil, *Renew. Sust. Energy Rev.* **2018**, *82*, 4159.
[17] Z. Liu, W. Gao, H. Oshima, K. Nagase, C.-H. Lee, T. Mori, *Nat. Commun.* **2022**, *13*, 1120.
[18] Q. Jin, S. Jiang, Y. Zhao, D. Wang, J. Qiu, D.-M. Tang, J. Tan, D.-M. Sun, P.-X. Hou, X.-Q. Chen, K. Tai, N. Gao, C. Liu, H.-M. Cheng, X. Jiang, *Nat. Mater.* **2019**, *18*, 62.
[19] F. Hao, P. Qiu, Y. Tang, S. Bai, T. Xing, H.-S. Chu, Q. Zhang, P. Lu, T. Zhang, D. Ren, J. Chen, X. Shi, L. Chen, *Energy Environ. Sci.* **2016**, *9*, 3120.
[20] J. Mao, G. Chen, Z. Ren, *Nat. Mater.* **2021**, *20*, 454.
[21] Z.-G. Chen, X. Shi, L.-D. Zhao, J. Zou, *Prog. Mater. Sci.* **2018**, *97*, 283.
[22] X. Zhang, Z. Bu, S. Lin, Z. Chen, W. Li, Y. Pei, *Joule* **2020**, *4*, 986.
[23] K. Zhao, P. Qiu, X. Shi, L. Chen, *Adv. Funct. Mater.* **2019**, *30*, 1903867.
[24] M. Dargusch, X.-L. Shi, X. Q. Tran, T. Feng, F. Somidin, X. Tan, W. Liu, K. Jack, J. Venezuela, H. Maeno, T. Toriyama, S. Matsumura, S. T. Pantelides, Z.-G. Chen, *J. Phys. Chem. Lett.* **2019**, *10*, 6512.
[25] M. Jin, X.-L. Shi, T. Feng, W. Liu, H. Feng, S. T. Pantelides, J. Jiang, Y. Chen, Y. Du, J. Zou, Z.-G. Chen, *ACS Appl. Mater. Interfaces* **2019**, *11*, 8051.
[26] Z.-Y. Liu, J.-L. Zhu, X. Tong, S. Niu, W.-Y. Zhao, *J. Adv. Ceram.* **2020**, *9*, 647.
[27] Y. Tang, Z. M. Gibbs, L. A. Agapito, G. Li, H. S. Kim, M. B. Nardelli, S. Curtarolo, G. J. Snyder, *Nat. Mater.* **2015**, *14*, 1223.
[28] X. Meng, Z. Liu, B. Cui, D. Qin, H. Geng, W. Cai, L. Fu, J. He, Z. Ren, J. Sui, *Adv. Energy Mater.* **2017**, *7*, 1602582.
[29] G. Rogl, A. Grytsiv, P. Rogl, E. Bauer, M. Hochenhofer, R. Anbalagan, R. C. Mallik, E. Schafler, *Acta Mater.* **2014**, *76*, 434.
[30] G. S. Nolas, M. Kaeser, R. T. Littleton, T. M. Tritt, *Appl. Phys. Lett.* **2000**, *77*, 1855.
[31] D. Bérardan, E. Alleno, C. Godart, M. Puyet, B. Lenoir, R. Lackner, E. Bauer, L. Girard, D. Ravot, *J. Appl. Phys.* **2005**, *98*, 033710.
[32] H. Y. Geng, S. Ochi, J. Q. Guo, *Appl. Phys. Lett.* **2007**, *91*, 022106.
[33] H. Li, X. Tang, X. Su, Q. Zhang, *Appl. Phys. Lett.* **2008**, *92*, 202114.
[34] H. Li, X. Tang, Q. Zhang, C. Uher, *Appl. Phys. Lett.* **2008**, *93*, 252109.
[35] J. Y. Peng, P. N. Alboni, J. He, B. Zhang, Z. Su, T. Holgate, N. Gothard, T. M. Tritt, *J. Appl. Phys.* **2008**, *104*, 053710.
[36] X. Shi, H. Kong, C. P. Li, C. Uher, J. Yang, J. R. Salvador, H. Wang, L. Chen, W. Zhang, *Appl. Phys. Lett.* **2008**, *92*, 182101.
[37] J. Graff, S. Zhu, T. Holgate, J. Peng, J. He, T. M. Tritt, *J. Electron. Mater.* **2011**, *40*, 696.
[38] K.-H. Park, W.-S. Seo, D.-K. Shin, I.-H. Kim, *J. Korean Phys. Soc.* **2014**, *65*, 491.
[39] B. Ryll, A. Schmitz, J. de Boor, A. Franz, P. S. Whitfield, M. Reehuis, A. Hoser, E. Müller, K. Habicht, K. Fritsch, *ACS Appl. Energy Mater.* **2018**, *1*, 113.
[40] W. Li, J. Wang, Y. Xie, J. L. Gray, J. J. Heremans, H. B. Kang, B. Poudel, S. T. Huxtable, S. Priya, *Chem. Mater.* **2019**, *31*, 862.

[41] D. Qin, W. Shi, Y. Lu, W. Cai, J. Sui, *ACS Appl. Mater. Interfaces* **2022**, *14*, 30901.
[42] Y. Tang, S.-w. Chen, G. J. Snyder, *J. Mater.* **2015**, *1*, 75.
[43] S.-w. Chen, J.-w. Chen, P.-h. Lin, *Mater. Lett.* **2016**, *182*, 36.
[44] S. Wang, J. R. Salvador, J. Yang, P. Wei, B. Duan, J. Yang, *NPG Asia Mater.* **2016**, *8*, e285.
[45] X. Song, J. Yang, J. Peng, Y. Chen, W. Zhu, T. Zhang, *J. Alloys Compd.* **2005**, *399*, 276.
[46] J. Yang, Y. Chen, W. Zhu, S. Bao, X.a.F. Xingkai Duan, *J. Am. Ceram. Soc.* **2011**, *94*, 277.
[47] Y. Tang, R. Hanus, S.-w. Chen, G. J. Snyder, *Nat. Commun.* **2015**, *6*, 7584.
[48] B. Alinejad, A. Castellero, M. Baricco, *Scr. Mater.* **2016**, *113*, 110.
[49] M. V. Daniel, C. Brombacher, G. Beddies, N. Jöhrmann, M. Hietschold, D. C. Johnson, Z. Aabdin, N. Peranio, O. Eibl, M. Albrecht, *J. Alloys Compd.* **2015**, *624*, 216.
[50] X.-G. Li, W.-D. Liu, S.-M. Li, D. Li, H. Zhong, Z.-G. Chen, *ACS Appl. Mater. Interfaces* **2021**, *13*, 54185.
[51] O. L. Arnache, J. Pino, L. C. Sánchez, *J. Mater. Sci.: Mater. Electrons* **2016**, *27*, 4120.
[52] L. Zhang, A. Grytsiv, M. Kerber, P. Rogl, E. Bauer, M. J. Zehetbauer, J. Wosik, G. E. Nauer, *J. Alloys Compd.* **2009**, *481*, 106.
[53] H. Zhu, S. Liang, T. Ouyang, S. Yue, J. Jiang, *J. Mater. Sci. Mater. Electrons* **2017**, *28*, 10509.
[54] M. B. A. Bashir, S. M. Said, M. F. M. Sabri, Y. Miyazaki, D. A. Shnawah, M. Shimada, M. F. M. Salleh, M. S. Mahmood, E. Y. Salih, F. Fitriani, M. H. Elsheikh, *J. Electron. Mater.* **2018**, *47*, 2429.
[55] O. Raihan, S. Mohd Said, M. F. M. Sabri, S. Rozali, B. D. Long, K. Kimura, K. Tobita, Fitriani, M. F. M. S., M. B. Ali Bashir, *Mater. Res. Express* **2018**, *5*, 105008.
[56] M. B. A. Bashir, M. F. Mohd Sabri, S. M. Said, Y. Miyazaki, I. A. Badruddin, D. A. Ameer Shnawah, E. Y. Salih, S. Abushousha, M. H. Elsheikh, *J. Solid State Chem.* **2020**, *284*, 121205.
[57] S. Meledath Valiyaveettil, D.-L. Nguyen, D. P. Wong, C.-R. Hsing, L. Paradis-Fortin, M. Qorbani, A. Sabbah, T.-L. Chou, K.-K. Wu, V. Rathinam, C.-M. Wei, L.-C. Chen, K.-H. Chen, *Inorg. Chem.* **2022**, *61*, 4442.
[58] W.-S. Liu, B.-P. Zhang, J.-F. Li, L.-D. Zhao, *J. Phys. D: Appl. Phys.* **2007**, *40*, 566.
[59] M. H. Elsheikh, M. F. M. Sabri, S. M. Said, Y. Miyazaki, H. H. Masjuki, D. A. A. Shnawah, B. D. Long, S. Naito, M. B. A. Bashir, *J. Electron. Mater.* **2016**, *45*, 2886.
[60] S. M. Said, M. B. A. Bashir, M. F. M. Sabri, Y. Miyazaki, D. A. A. Shnawah, A. S. Hakeem, M. Shimada, A. I. Bakare, N. N. N. Ghazali, M. H. Elsheikh, *Metall. Mater. Trans. A* **2017**, *48*, 3073.
[61] D. Qin, B. Cui, X. Meng, P. Qin, L. Xie, Q. Zhang, W. Liu, J. Cao, W. Cai, J. Sui, *Mater. Today Phys.* **2019**, *8*, 128.
[62] D. Qin, H. Wu, S. Cai, J. Zhu, B. Cui, L. Yin, H. Qin, W. Shi, Y. Zhang, Q. Zhang, W. Liu, J. Cao, S. J. Pennycook, W. Cai, J. Sui, *Adv. Energy Mater.* **2019**, *9*, 1902435.
[63] G. Nie, W. Li, J. Guo, A. Yamamoto, K. Kimura, X. Zhang, E. B. Isaacs, V. Dravid, C. Wolverton, M. G. Kanatzidis, S. Priya, *Nano Energy* **2019**, *66*, 104193.
[64] R. He, S. Gahlawat, C. Guo, S. Chen, T. Dahal, H. Zhang, W. Liu, Q. Zhang, E. Chere, K. White, Z. Ren, *Phys. Status Solidi A* **2015**, *212*, 2191.
[65] M. Battabyal, B. Priyadarshini, D. Sivaprahasam, N. S. Karthiselva, R. Gopalan, *J. Phys. D: Appl. Phys.* **2015**, *48*, 455309.
[66] T. Dahal, H. S. Kim, S. Gahlawat, K. Dahal, Q. Jie, W. Liu, Y. Lan, K. White, Z. Ren, *Acta Mater.* **2016**, *117*, 13.
[67] R. He, S. Gahlawat, C. Guo, S. Chen, T. Dahal, H. Zhang, W. Liu, Q. Zhang, E. Chere, K. White, *Phys. Status Solidi A* **2015**, *212*, 2191.
[68] X.-L. Shi, W.-D. Liu, M. Li, Q. Sun, S.-D. Xu, D. Du, J. Zou, Z.-G. Chen, *Adv. Energy Mater.* **2022**, *12*, 2200670.
[69] K. Tyagi, B. Gahtori, S. Bathula, M. Jayasimhadri, S. Sharma, N. K. Singh, D. Haranath, A. K. Srivastava, A. Dhar, *Solid State Commun.* **2015**, *207*, 21.
[70] Y. Jin, X. Zhang, Y. Xiao, W. He, D. Wang, J. Li, S. Zheng, D. Ren, Y. Qiu, L.-D. Zhao, *Scr. Mater.* **2020**, *183*, 22.
[71] K. Tyagi, B. Gahtori, S. Bathula, V. Toutam, S. Sharma, N. K. Singh, A. Dhar, *Appl. Phys. Lett.* **2014**, *105*, 261902.
[72] Z. Liu, W. Gao, X. Meng, X. Li, J. Mao, Y. Wang, J. Shuai, W. Cai, Z. Ren, J. Sui, *Scr. Mater.* **2017**, *127*, 72.
[73] H. Anno, M. Hokazono, R. Shirataki, Y. Nagami, *J. Electron. Mater.* **2013**, *42*, 2326.
[74] F. Tseng, S. Li, C. Wu, Y. Pan, L. Li, *J. Mater. Sci.* **2016**, *51*, 5271.
[75] K. Ueno, A. Yamamoto, T. Noguchi, T. Inoue, S. Sodeoka, H. Obara, *J. Alloys Compd.* **2005**, *388*, 118.
[76] L. Zhao, X. Wang, F. Y. Fei, J. Wang, Z. Cheng, S. Dou, J. Wang, G. J. Snyder, *J. Mater. Chem. A* **2015**, *3*, 9432.
[77] J. Davidow, Y. Gelbstein, *J. Electron. Mater.* **2013**, *42*, 1542.
[78] J. R. Salvador, J. Yang, X. Shi, H. Wang, A. A. Wereszczak, *J. Solid State Chem.* **2009**, *182*, 2088.
[79] S. Perumal, S. Roychowdhury, D. S. Negi, R. Datta, K. Biswas, *Chem. Mater.* **2015**, *27*, 7171.
[80] R. D. Schmidt, E. D. Case, J. Giles, J. E. Ni, T. P. Hogan, *J. Electron. Mater.* **2012**, *41*, 1210.
[81] R. D. Schmidt, E. D. Case, L.-D. Zhao, M. G. Kanatzidis, *J. Mater. Sci.* **2015**, *50*, 1770.
[82] A. Kosuga, S. Urata, K. Kurosaki, S. Yamanaka, R. Funahashi, *Jpn. J. Appl. Phys.* **2008**, *47*, 6399.
[83] H. W. Kerr, W. Kurz, *Int. Mater. Rev.* **1996**, *41*, 129.
[84] W.-S. Liu, B.-P. Zhang, J.-F. Li, L.-D. Zhao, *J. Phys. D Appl. Phys.* **2007**, *40*, 6784.